



# CHORUS

This is the accepted manuscript made available via CHORUS. The article has been published as:

## Pressure effect on the electronic, structural, and vibrational properties of layered 2H-MoTe<sub>2</sub>

Xiao-Miao Zhao, Han-yu Liu, Alexander F. Goncharov, Zhi-Wei Zhao, Viktor V. Struzhkin, Ho-Kwang Mao, Alexander G. Gavriliuk, and Xiao-Jia Chen

Phys. Rev. B **99**, 024111 — Published 28 January 2019

DOI: [10.1103/PhysRevB.99.024111](https://doi.org/10.1103/PhysRevB.99.024111)

# Pressure effect on electronic, structural, and vibrational properties of layered $2H$ -MoTe<sub>2</sub>

Xiao-Miao Zhao,<sup>1,2,3</sup> Han-yu Liu,<sup>3</sup> Alexander F. Goncharov,<sup>3</sup> Zhi-Wei Zhao,<sup>2</sup> Viktor V. Struzhkin,<sup>3</sup> Ho-Kwang Mao,<sup>3,1</sup> Alexander G. Gavriliuk,<sup>4,5</sup> and Xiao-Jia Chen<sup>1,6,3,\*</sup>

<sup>1</sup>Center for High Pressure Science and Technology Advanced Research, Shanghai 201203, China

<sup>2</sup>College of Materials Science and Engineering, Henan University of Technology, Zhengzhou 450001, China

<sup>3</sup>Geophysical Laboratory, Carnegie Institution of Washington, Washington, DC 20015, U.S.A.

<sup>4</sup>Institute of Crystallography, Russian Academy of Sciences, Leninsky pr. 59, Moscow 119333, Russia

<sup>5</sup>Institute for Nuclear Research, Russian Academy of Sciences, Troitsk, Moscow 142190, Russia

<sup>6</sup>Key Laboratory of Materials Physics, Institute of Solid State Physics, Chinese Academy of Science, Hefei 230031, China

(Dated: January 10, 2019)

Layered molybdenum dichalcogenides differ from the classic example of bilayer graphene with their unique electronic properties, the application of pressure can continuously tune electronic structure since the band gap is controlled by delicate interlayer interaction. Here, we have performed measurements of Raman scattering, synchrotron X-ray diffraction, electrical conductivity measurements, and Hall coefficient combined with density functional theory calculations to synthetically study the pressure effect on  $2H$ -MoTe<sub>2</sub>. Both the experiments and calculations consistently demonstrate that MoTe<sub>2</sub> undergoes a semiconductor-to-metallic (S-M) transition above 10 GPa. Unlike MoS<sub>2</sub>, the S-M transition is driven by the gradual tunability of electric structure and band gap without structural transition. The applied pressure also effectively enhances conductivity and carrier concentration while reducing the mobility, which makes MoTe<sub>2</sub> more suitable for applications than most other transition-metal dichalcogenides and allows it to be applied in strain-modulated optoelectronic devices.

PACS numbers: 73.63.Bd, 64.70.Nd, 74.70.Ad, 74.62.Fj

## I. INTRODUCTION

Hexagonal transition metal dichalcogenides (TMDs) have stimulated widespread research interests among scientists and engineers because of unique electronic structure and attractive properties, which make them diverse applications such as valley-optoelectronics<sup>1-5</sup>, logic transistors<sup>6-8</sup>, spintronics<sup>9</sup>, and catalysis<sup>10</sup>. Different from the metallic graphene with zero-bandgap, these materials are used for electrodes in high-efficiency photoelectrochemical cells since the optical band gaps are matching well with the solar spectrum<sup>11</sup>. TMDs share a common structure consisting of a sheet of metallic atoms sandwiched between two layers of chalcogen atoms, but present multiple structural phases due to the different atomic coordination such as  $1T$ ,  $2H$ , and  $3R$ . In contrast to  $1T$  phase, which possesses a light band overlap near the Fermi level, even superconductivity at low temperature<sup>12-14</sup>, the  $2H$  phase has a large band gap and is stable at room temperature<sup>15-17</sup>. The indirect-to-direct band gap crossover can be achieved in  $2H$  phase when it is thinned down to the monolayer limit<sup>18</sup>. In addition to this atomically thin TMDs films have potential for the valley-based electronic and optoelectronic applications due to the valley polarization properties<sup>19</sup>.

As a member of the TMDs family,  $2H$ -MoTe<sub>2</sub> possesses interest features and is appealing for 2D electronics. Both the strong absorption throughout solar spectrum and strong spin-orbit coupling than other Mo-related TMD materials suggest that MoTe<sub>2</sub> is ideal ma-

terial for valleytronic devices<sup>20,21</sup>. MoTe<sub>2</sub> with a favorable band gap of  $\sim 1.0$  eV, which is quite close to that of bulk silicon ( $\sim 1.1$  eV), is beneficial in tuning field-effect transistors<sup>22</sup> and can extend the operating range of optoelectronic devices from the visible to the near-infrared range<sup>23,24</sup>. Furthermore, MoTe<sub>2</sub> has unique structural properties, structural phase transition from the  $\alpha$ -phase diamagnetic semiconductor to the  $\beta$ -phase paramagnetic metal can be induced by laser irradiation, achieving a true two-dimension device with an ohmic contact<sup>25</sup>. Additionally, superconductivity can be induced in MoTe<sub>2</sub> by ionic gating<sup>26</sup>. Except for heating and charge-carrier doping, high pressure is proved to be clean and powerful way to tune structural and electronic properties. Previous studies report that MoS<sub>2</sub> undergoes semiconducting to metallic phase transition under pressure<sup>27,28</sup>, and becomes a superconductor at high pressures<sup>29</sup>. Furthermore, theoretical studies<sup>30,31</sup> suggest that MoTe<sub>2</sub> with the similar crystal and electronic structure presents metallization and superconductivity under pressure, no experimental evidence is presented until now.

We herein extensively explore the high-pressure behavior of MoTe<sub>2</sub> by using X-ray diffraction, Raman spectroscopy, and electrical conductivity measurements. We examine the semiconductor to metallic transition occurred at about 10 GPa. Distinct from MoS<sub>2</sub>, the band gap of MoTe<sub>2</sub> closes gradually, and this transition without iso-structural phase transition is induced by the increasing interlayer interactions and Te-Te interactions through the first principles calculations. The conductiv-

ity, carrier concentration, and the mobility of MoTe<sub>2</sub> under pressure for the first time are measured and discussed in the letter. The wide modulation of charge transport properties renders MoTe<sub>2</sub> will be a promising material for optoelectronic applications under pressure.

## II. DETAIL METHODS

High-quality single crystals of 2H-MoTe<sub>2</sub> were synthesized at HQ Graphene. High pressure electrical transport and Hall coefficient measurements were conducted using the standard four-probe method in Quantum Designs Physical Property Measurement System by using a miniature nonmagnetic diamond anvil cell.<sup>32</sup> The diamond was 300  $\mu\text{m}$  in diameter and a thin BN layer acted as an electric insulator between the electrodes leads and the gasket. Four Pt wires were adhered to the sample using the silver epoxy, and Daphne oil 7373 was employed as a pressure-transmitting medium.

Diamond anvil cells with rhenium stainless steel gasket were used with the anvils in 300  $\mu\text{m}$  culet for both XRD and Raman spectroscopy measurements. The XRD experiments at high pressures with synchrotron radiation were performed at the Advanced Light Source (ALS) with a wavelength 0.4132  $\text{\AA}$ . Silicone oil was loaded as pressure transmitting medium to maintain quasi-hydrostatic pressure environment for XRD experiments. The pressure was determined from the shift of the luminescence of a ruby sphere enclosed in the sample.<sup>33</sup> The two-dimensional diffraction images were integrated into one-dimensional diffraction patterns through Fit 2D program. The Rietveld fitting was performed using GSAS package. The Raman spectra were measured in backscattering geometry with visible laser wavelength of 488 nm.

Total energy calculations and electronic property calculations were performed using density functional theory as implemented in the VASP code<sup>34</sup>. The projector augmented wave (PAW)<sup>35</sup> potentials for valence electrons were adopted for all simulations. The Perdew Burke Ernzerhof (PBE)<sup>36</sup> generalized gradient approximation (GGA)<sup>37</sup> was adopted as the exchange-correlation functional. A plane wave kinetic energy cutoff of 400 eV and appropriate Monkhost-Pack k-meshes with grid spacing of 0.03  $\text{\AA}^{-1}$  were chosen to ensure that total energy calculations are well converged.

## III. RESULTS AND DISCUSSION

The electronic transport measurements of MoTe<sub>2</sub> were conducted up to 41.7 GPa. Figure 1 (a) shows the temperature dependence of resistivity under various pressures. The resistivity exhibits the behavior of semiconductor at lower pressure, upon compression, the measured electrical resistivity shows a gradual decrease with the increase of pressure and ultimately undergoes a metallization at pressures above 9.6 GPa. The measure-

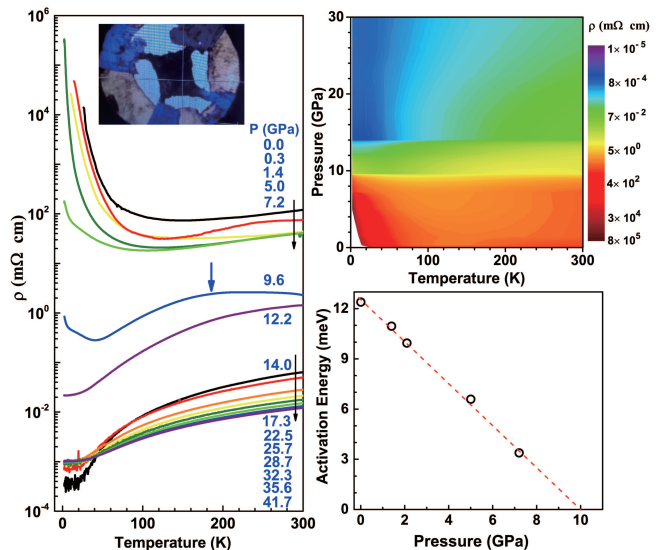


FIG. 1: (Color online) MoTe<sub>2</sub> transport measurements as a function of pressure. (a) Electrical resistance of MoTe<sub>2</sub> as a function of temperature at various pressures up to 41.7 GPa. (b) Temperature-pressure contour plot of resistivity showing the transition region from the semiconductor to metallic region that is derived from experimental electrical conductivity measurements. (c) Activation energy versus pressure, the line is fitted result.

ments exhibits that the semiconductor to metal transition occurs over a pressure-temperature range that is intermediate between the two states. For 9.6 GPa, the temperature-resistivity curves above 40 K shows positive  $d\rho/dT$ , whereas the low-temperature region has negative  $d\rho/dT$ , indicating the presence of a semiconducting state. At pressures above 12.2 GPa, positive  $d\rho/dT$  is observed at all temperatures, reflective of the metallization of MoTe<sub>2</sub>. In order to have a thorough study on MoTe<sub>2</sub>, the temperature dependence of resistivity at various pressures were measured as low as to 2 K, as shown in Fig. 1 (b). Within the whole study pressure region, the electrical resistivity presents a very large tunable range with the almost 10-order magnitude decrease from the semiconducting to metallic state. Although the resistivity profiles as a function of temperature at different pressures are similar, however, the change of resistance values are different due to the thermally activated carriers. The activation energy can be obtained by using the fit,  $R \propto E_a/2k_B T$ , in the temperature range between 50 K and 100 K, where  $R$  is the electrical resistance,  $k_B$  is Boltzmann's constant, and  $E_a$  is activation energy. The pressure dependence of the extracted activation energy can be analytically modeled as  $E_a = 32.4 - 19.9e^{0.05P}$ , as shown in Fig. 1(c). The effective defect energy level in the band gap that typically contributes mobile carriers is directly related to the activity energy, and as the band gap closes, the activation energy closes to zero. The fitting results demonstrate that the band gap will close at 9.3 GPa, which is in good agreement with the onset of metallization at 9.6 GPa from the measurements

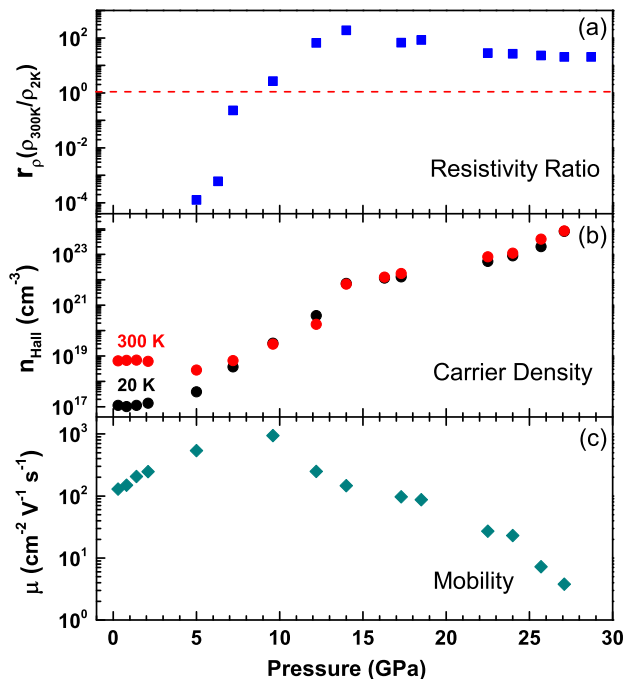


FIG. 2: (Color online) Pressure-dependent electronic carrier dynamics of MoTe<sub>2</sub>. (a) The resistivity ratio ( $r_\rho$ ) at pressures above 10.0 GPa is  $> 1$ , which indicates the onset of metallization, whereas  $r_\rho < 1$  is observed at lower pressures. The horizontal dashed line demarcates the electronic transition between the semiconducting and the metallic states. (b) The carrier density presented 5 orders increase from  $10^{19} \text{ cm}^{-3}$  to  $10^{24} \text{ cm}^{-3}$  in the semiconductor and metallic regions, respectively. (c) The Hall mobility increases slightly in semiconducting state, then decreases in metallic state.

of resistivity. Unlike the abrupt drop in resistivity for MoS<sub>2</sub><sup>28</sup>, MoTe<sub>2</sub> exhibits a gradual decrease in resistivity and band gap, similar to MoSe<sub>2</sub><sup>38</sup> and WS<sub>2</sub><sup>39</sup>. There is a broad hump occurred in  $R$ - $T$  curve (marked by arrow), similar behavior is observed in MoS<sub>2</sub>, Chi<sup>29</sup> and Cao<sup>40</sup> speculated that this anomaly is associated with the formation of charge density wave, which plays an important role in facilitating the emergence of superconductivity. In Comparison with MoSe<sub>2</sub> and WS<sub>2</sub>, the semiconducting to metal transition of MoTe<sub>2</sub> undergoes a narrower pressure-temperature range, and MoTe<sub>2</sub> can achieve the metallization above 9.6 GPa, which is lower than 22 GPa for WS<sub>2</sub> and 27 GPa for MoSe<sub>2</sub>. In addition, multilayered WS<sub>2</sub> shows a 6-order magnitude increase in resistivity from the semiconducting to metallic state, whereas MoTe<sub>2</sub> presents a very larger tunable range with the almost 10-order magnitude decrease in resistivity, which allows MoTe<sub>2</sub> to be applied in opto-electronics.

With the increase of pressure, a gradual decrease in resistivity is observed. The value of resistivity ratio,  $\rho_{300K}/\rho_{2K}$ , can be used to check the onset of metallization. The transition of the resistivity ratio  $r_\rho$  from values smaller than 1 to values larger than 1 means the onset of metallization. As seen in Fig 2(a), the value of resistiv-

ity ratio is larger than 1 above 9.6 GPa, indicating the beginning of metallization. In order to detailed probing the properties of electronic carrier of MoTe<sub>2</sub> under pressure, high pressure Hall resistance were measured with a magnetic field perpendicular to the  $a$ - $b$  plane of the single crystal. The estimated carrier concentration  $n_H$  at 20 K and 300 K as a function of pressure are shown in Fig. 2(b). At low pressure, the carrier concentration  $n_H$  at 20 K is lower than that at 300 K. With the increasing pressure, there is a 5-order magnitude increase in carrier concentration at 20 K from ambient pressure to 30 GPa. In comparison to previous reported WS<sub>2</sub><sup>39</sup> with 4 order magnitude of tunability, MoTe<sub>2</sub> possesses a larger tunable range. Furthermore, the Hall carrier mobility,  $\mu = |Rh|/\rho$ , can be estimated based on the measured Hall coefficient. The calculated Hall carrier mobility of MoTe<sub>2</sub> is  $129 \text{ cm}^2 \text{V}^{-1} \text{s}^{-1}$  at ambient pressure and room temperature, which is larger than the field-effect mobility of  $20 \text{ cm}^2 \text{V}^{-1} \text{s}^{-1}$ .<sup>41</sup> The Hall carrier mobility is usually higher than the field-effect mobility, which suffers from additional transport effects such as contact resistance and gate-oxide interface scattering<sup>42,43</sup>. The Hall carrier mobility of MoTe<sub>2</sub> at ambient pressure is comparable to other TMDs such as MoSe<sub>2</sub> ( $100 - 160 \text{ cm}^2 \text{V}^{-1} \text{s}^{-1}$ )<sup>44</sup>. Note that the Hall carrier mobility is increased with increasing pressure from ambient pressure to 9.6 GPa, then it drops gradually by applied pressure with almost 3-order magnitude. After enter the metallic state, the decrease in Hall carrier mobility may associate to the pressure-induced doping when the free carrier scatter within the confined lattice more frequently, therefore leading to a decrease in drift velocity.

Electronic transition such as insulator to metal or semiconductor to metal transitions are usually accompanied or followed by structural transition or atomic movements take place. Raman spectroscopy is known to be a powerful tool for the investigation of both chemical reactivity and even subtle structural distortion. We measured high pressure Raman spectra of MoTe<sub>2</sub> up to 51 GPa, as shown in Fig. 2 (a). The irreducible representations for  $2H$ -MoTe<sub>2</sub> are  $\Gamma = E_{2g}^2 + E_{1g} + A_{1g} + E_{2g}^1$ <sup>45</sup>. The four eigenvectors:  $29 \text{ cm}^{-1}$  ( $E_{2g}^2$ -derived),  $117 \text{ cm}^{-1}$  ( $E_{1g}$ -derived),  $175 \text{ cm}^{-1}$  ( $A_{1g}$ -derived), and  $232 \text{ cm}^{-1}$  ( $E_{2g}^1$ -derived) are shown in the top of Fig. 1(a). The Raman modes observed in our study are in good agreement with previous reports. With the increasing pressure, the  $E_{1g}$  mode cannot be observed from both previous reports and our measurements, which may due to the weak intensity. The intensity of  $E_{2g}^2$  mode gradually increase as pressure is increased. All the Raman modes shift toward higher frequencies with the application of pressure. No obvious phase transition can be detected over the pressure region studied. The detailed pressure-dependence of the phonon frequencies of MoTe<sub>2</sub> are plotted shown in Fig. 2(b). Upon compression to about 10 GPa, one can clear see that these Raman modes have an obvious discontinuities in the pressure shift and changes in the rate of shift verse pressure, coinciding with the pressure

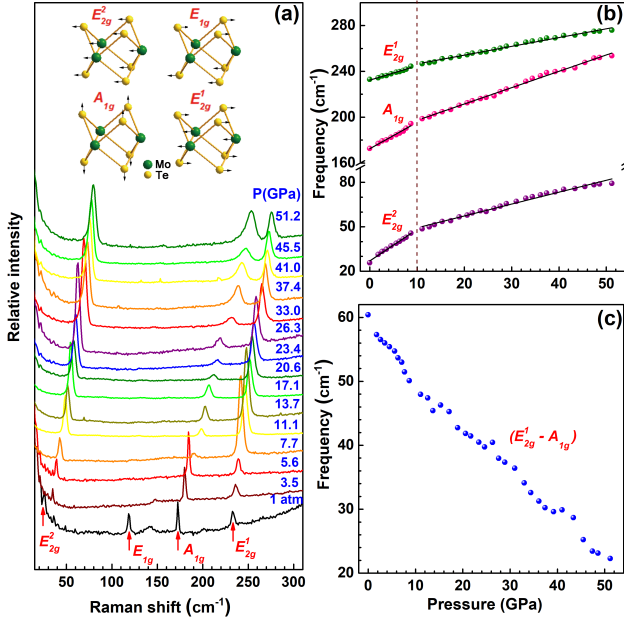


FIG. 3: (Color online) (a) Raman spectra of MoTe<sub>2</sub> at various pressures up to 51.2 GPa in the compression run. The insets represent in plane phonon modes  $E_{2g}^2$ ,  $E_{1g}^1$ , and  $E_{2g}^1$  and the out-of-plane phonon mode  $A_{1g}$ . (b) Phonon frequencies of MoTe<sub>2</sub> as a function of pressure. (c) Evolution of vibrational modes  $A_{1g}$  and  $E_{2g}^2$ , and their difference ( $E_{2g}^2 - A_{1g}$ ) under pressure, measured by Raman spectroscopy.

of the onset of metallization. For the in-plane mode  $E_{2g}^2$ , its  $d\nu/dP$  is obviously smaller than that below 10 GPa. With increasing pressure, the increase of the  $E_{2g}^1$  mode is smaller than that of  $A_{1g}$ , thus these two modes  $E_{1g}^1$  and  $A_{1g}$  are close to each other. As seen in Fig. 3(c), the frequency difference between these two modes has been plotted out. The frequency difference is strongly decreased from 60  $\text{cm}^{-1}$  at ambient pressure to 20  $\text{cm}^{-1}$  at 51.2 GPa and will be close to zero at higher pressure. There are similar cases occurred in other TMDs<sup>38,39</sup>, it is explained that the crystal structure continuously evolves from a quasi-two-dimensional structure to an isotropic three-dimensional structure.

To further explore the structural evolution of MoTe<sub>2</sub> under pressure, high pressure X-ray diffraction measurements were performed up to 45.2 GPa. Figure 4 (a) shows some representative XRD patterns collected under various pressures for both compression and decompression runs. When looking at the evolution of the diffraction patterns as a function of applied pressure the peak positions shift to higher angles as the crystal structure is compressed. No dramatic changes can be observed in XRD patterns except for the gradually decrease in intensity of some peaks, which may due to the weak signal at high pressures resulting from gradually decreasing thickness. Upon decompression, we observed that it is reversible. For MoS<sub>2</sub>, the distinct features from Raman and XRD demonstrate that it undergoes the iso-structural transition from  $2H_c$  to  $2H_a$  with the application of pressure.

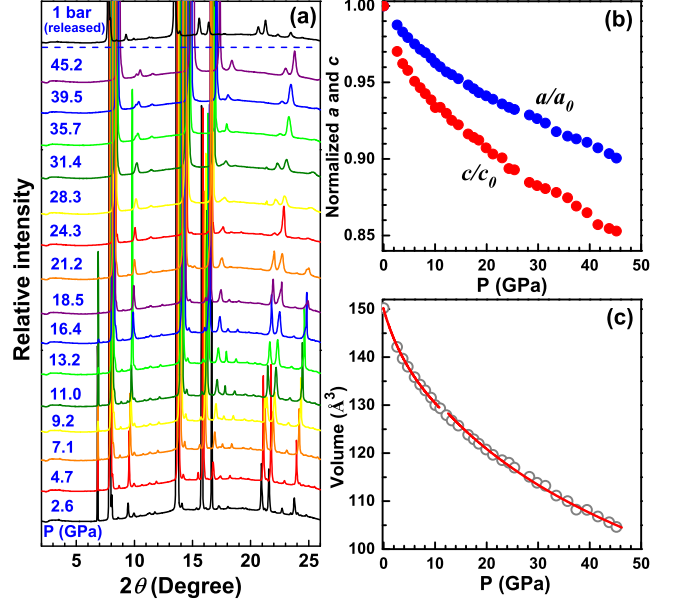


FIG. 4: (Color online) Structural properties of the MoTe<sub>2</sub> at high pressures. (a) Synchrotron X-ray diffraction patterns of MoTe<sub>2</sub> during the pressurization from 2.6 to 45.2 GPa. (b) Normalized cell parameters  $a/a_0$  and  $c/c_0$  versus pressure. (c) The volume of MoTe<sub>2</sub> as a function of pressure. Solid lines represent the fitting results to the equation of states.

MoTe<sub>2</sub> and MoS<sub>2</sub> is iso-structural crystal structures and possess highly similar electric structures at ambient condition, reminiscent of the same transition occurred in MoTe<sub>2</sub> under pressure. However, we do not find the evidence of the transition from  $2H_c$  to  $2H_a$  up to 50 GPa for MoTe<sub>2</sub>. The *ab initio* calculations<sup>38,46</sup> indicate that MoX<sub>2</sub> (X = S, Se, and Te) needs to overcome an energy barrier to undergo the transition from  $2H_c$  to  $2H_a$ , the maximum energy barrier is 0.5 eV for MoTe<sub>2</sub>, which is much higher than that of 0.15 eV for MoS<sub>2</sub>. Additionally, it is unfavorable to undergo the transition since the  $2H_a$  phase bear higher energies than the initial  $2H_c$  phase. The  $2H_c$  phase is more stable than  $2H_a$  phase for MoTe<sub>2</sub>, similar to  $2H$ -MoSe<sub>2</sub>.

All the refinements of diffraction patterns up to 45.2 GPa were carried out to obtain the lattice parameters at high pressure. The refined lattice parameters and the unit cell volume as a function of pressure are shown in Fig. 4(b-c) together with the experimental data at ambient pressure from previous report. The *c*-axis is more compressible than *a*-axis at lower pressure due to the weak vdW interactions in between Te-Te layers. With the increasing pressure, the interlayer interactions and Te-Te interactions are increased, the *c*-axis becomes much less compressible at higher pressure. Over the entire pressure range studies, the *c*-axis and *a*-axis is decreased by 15% and 10%, respectively. A third-order Birch-Murnaghan (BM) equation of state (EOS)<sup>47</sup> is employed to fit the volume-pressure relationship. Although the pressure dependence of volume does not show any discontinuity and sudden drop from semiconducting state to metallic state,

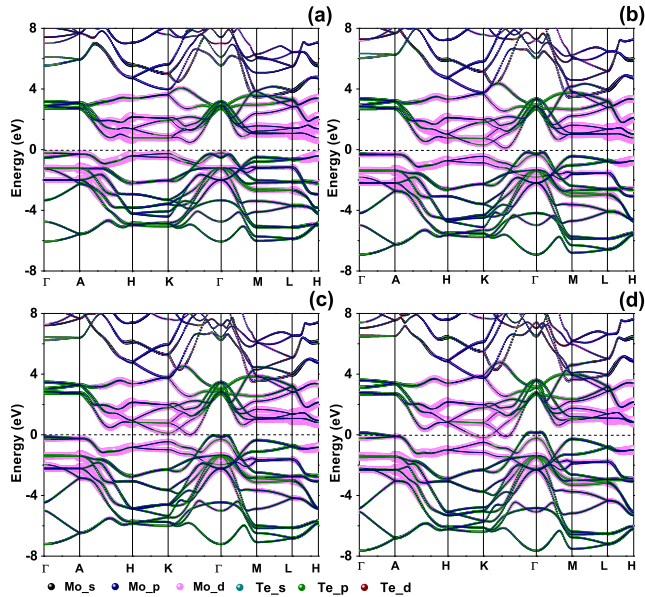


FIG. 5: (Color online) Calculated band structures of MoTe<sub>2</sub>. (a) Ambient pressure, (b) 7 GPa, (c) 10 GPa, and (d) 15 GPa. Black dotted line shows the Fermi level ( $E_F$ ).

the metallic state displays a distinct EOS behavior from that of semiconducting state, similar case occurred in other TMDs such as WS<sub>2</sub>. Fitting our data in semiconducting state, we obtained the ambient pressure bulk modulus  $K_0$  of 39.41(5) GPa with its first pressure derivative  $K_0' = 9.06(1)$ , and the ambient pressure volume  $V_0 = 149.99(1)$ , and the fit to the data within the metallic phase results in the value of  $K_0 = 65.91(15)$ ,  $K_0' = 4.03(1)$ , and  $V_0 = 147.91(6)$ , where the value of  $K_0$  in metallic state is bigger than that of semiconducting state, indicating that the metallic state is less compressible than semiconducting state. The different compressibility between two states should be responsible for the different  $d\nu/dP$  for Raman modes.

To understand the electronic behavior of MoTe<sub>2</sub> under pressure, we calculated the electronic band structure by using density functional theory at various pressures. The optimized lattice parameters are in good agreement with experimental results. In Fig. 5, we present the band structures of MoTe<sub>2</sub> as various pressures. We note that the fundamental band gap at ambient pressure is an indirect gap between the valence-band (VB) maximum at  $\Gamma$  and the conduction-band (CB) minimum, which lies between  $\Gamma$  and K. The band diagram shows an indirect (direct) band gap of 0.71 (1.04) eV at ambient pressure. It is apparent at a glance that the band gap becomes narrow gradually and is driven continuously to zero with increasing pressure due to the decrease of the interlayer distance, and band overlap begins at 10 GPa between the valance band top, slightly displaced from  $\Gamma$ , and the conduction band bottom, which lies between  $\Gamma$  and K. The band diagram is very similar to the multilayered MoS<sub>2</sub>, which metalizes after the formation of 2- $H_a$  phase.<sup>27</sup> The electronic structural calculations are consistent with ex-

perimental measurements where the onset of metallization takes place at 9.6 GPa with positive  $d\rho/dT$  above 40 K. The contribution from different orbits are marked with different colors in Fig. 5, we can clearly see that the bottom of CB mainly origins from the Mo  $d$  orbit, and the top of the VB mainly comes from Mo  $p$  and Te  $p$  orbits. For MoSe<sub>2</sub><sup>38</sup>, high pressure induces larger movements of the orbitals towards the  $E_F$ , leading to two CB valley minimum, one is  $dxz$  and  $dyz$  dominated CB at K point, the other one between  $\Gamma$  and K mainly comes from the Mo  $dxz$  and  $dx^2 - y^2$ . The top of VBs origins from the Mo  $dz^2$  orbital. With the increase of pressure, there are two nearly degenerate maximum on VB located close to  $\Gamma$  point for MoTe<sub>2</sub>. With increasing pressure, both the CBs and VBs shift their energy due to the increased interlayer electronic coupling, similar to MoS<sub>2</sub>. At 15 GPa, the CB minima and VB maxima cross the Fermi level, indicating a complete metallization, it is noteworthy that the energy level of the CB at K point shifts significantly downward with pressure, and the CB minimum shifts to the K point in metallize state (see Fig. 5d). Similar to other TMDs, the shifts of CBs and VBs driven by pressure generate a number of electron pockets and hole pocket. Because Te possesses the larger atom radius and has broader electron orbitals than Se and S, which may yield that the pressure of metallization of MoTe<sub>2</sub> is less than most other TMDs, such as MoS<sub>2</sub>, MoSe<sub>2</sub>, and WS<sub>2</sub>.

#### IV. CONCLUSIONS

In conclusion, we have studied the structural, vibrational, and electronic properties of high-pressure 2H-MoTe<sub>2</sub> by using multiple experimental techniques and first-principles *ab initio* calculations. We found a continuous transition from semiconductor to metallic transition take place at about 10 GPa. Unlike the isostructural transition of MoS<sub>2</sub>, XRD measurements indicate there is no structural transition during S-M transition, the discontinuities of Raman shifts at 10 GPa is interpreted in terms of the change of compressibility. Both the resistivity and band gap show a gradually by the application of pressure due to the increase of interlayer interactions and Te-Te interactions. In particular, the pressure of metallization for MoTe<sub>2</sub> is lower to most other TMDs, and MoTe<sub>2</sub> possesses highly tunable transport properties under pressure including the almost 10 orders of magnitude decrease in resistivity, 5 orders increase in carrier concentration, and 3 orders decrease in mobility. These studies expand the known space of layered materials with widely tunable band gaps beyond the classic example of bilayer graphene and suggest the promise future developments in strain-modulated optoelectronics devices. One may be concerned that the possible superconductivity of MoTe<sub>2</sub> will be achieved driven by higher pressure than reported here as the case of multilayered MoS<sub>2</sub>.

## Acknowledgments

This project was supported by the Doctoral Fund of Henan University of Technology under Grant No. 2018BS004 and the Fundamental Research Funds for the Henan Provincial Colleges and University of Technology under Grant No. 2018QNJH29. This structure measurements were supported by the Cultivation Fund of the Key Scientific and Technical Innovation Project Ministry of

Education of China (Project No.708070). The electrical transport measurements were supported by the DOE under Grant No.DE-FG02-02ER45955. Use of the BSRF for XRD measurements was supported by the Chinese Academy of Sciences. A.G.G. acknowledges the support from Russian Foundation for Basic Research grant 14-02-00483-a, from RAS programs “Strongly correlated electron systems”, “Elementary particle physics, fundamental nuclear physics and nuclear technologies”.

- 
- \* Electronic address: xjchen@hpstar.ac.cn
- <sup>1</sup> Q. H. Wang, K. Kalantar-Zadeh, A. Kis, J. N. Coleman, M. S. Strano, *M. S. Nat. Nanotechnol.*, **7**, 699 (2012).
  - <sup>2</sup> B. Radisavljevic, A. Radenovic, J. Brivio, V. Giacometti, A. Kis, *Nat. Nanotechnol.* **6**, 147(2011).
  - <sup>3</sup> L. Britnell, R. M. Ribeiro, A. Eckmann, R. Jalil, B. D. Belle, A. Mishchenko, Y. J. Kim, R. V. Gorbachev, S. V. Morozov, A. N. Geim, C. Casiraghi, A. H. Castro Neto, K. S. Novoselov, *Science*, **340**, 1311 (2013).
  - <sup>4</sup> R. S. Sundaram, M. Engel, A. Lombardo, R. Krupke, A. C. Ferrari, Ph. Avouris, and M. Steiner, *Nano Lett.* **34013**, 1416(2013).
  - <sup>5</sup> Y. F. Lin, Y. Xu, S. T. Wang, S. L. Li, M. Yamamoto, A. Aparecido-Ferreira, W. Li, H. Sun, S. Nakaharai, W. B. Jian, K. J. Ueno, K. Tsukagoshi, *Adv. Mater.* **26**, 3263 (2014).
  - <sup>6</sup> Y. Yoon, K. Ganapathi, S. Salahuddin, *Nano Lett.* **11**, 3768(2011).
  - <sup>7</sup> S. Kim, A. Konar, W. S. Hwang, J. H. Lee, J. Lee, J. Yang, C. Jung, H. Kim, J. B. Yoo, J. Y. Choi, Y. M. Jin, S. Y. Lee, D. Jena, W. Choi, and K. Kim, *Nat. Commun.* **3**, 1(2012).
  - <sup>8</sup> S. Das, A. Prakash, R. Salazar, J. Appenzeller, *ACS Nano* **8**, 1681 (2014).
  - <sup>9</sup> X. Xu, W. Yao, D. Xiao, T. E. Heinz, *Nat. Phys.* **10**, 343 (2014).
  - <sup>10</sup> M. A. Lukowski, A. S. Daniel, F. Meng, A. Forticaux, L. Li, S. Jin, *J. Am. Chem. Soc.* **135**, 10274 (2013).
  - <sup>11</sup> H. D. Abruña, G. A. Hope, A. J. Bard, *J. Electrochem. Soc.* **129**, 2224 (1982).
  - <sup>12</sup> D. Kang, Y. Zhou, W. Yi, C. Yang, J. Guo, Y. Shi, S. Zhang, Z. Wang, C. Zhang, S. Jiang, A. Li, K. Yang, Q. Wu, G. Zhang, L. Sun, and Z. Zhao. *Nat. Commun.*, **6**, 7804.(2015).
  - <sup>13</sup> X. Pan, X. Chen, H. Liu, Y. Feng, Z. Wei, Y. Zhou, Z. Chi, L. Pi, F. Yen, F. Song, X. Wan, Z. Yang, B. Wang, G. Wang, and Y. Zhang. *Nat. Commun.*, **6**, 7805 (2015).
  - <sup>14</sup> Y. Qi, P. G. Naumov, M. N. Ali, C. R. Rajamathi, W. Schnelle, O. Barkalov, M. Hanfland, S. Wu, C. Shekhar, Y. Sun, V. Süß, M. Schmidt, U. Schwarz, E. Pippel, P. Werner, R. Hillebrand, T. Förster, E. Kampert, S. Parkin, R. J. Cava, C. Felser, B. Yan, and S. A. Medvedev. *Nat. Commun.*, **7**, 11038 (2016).
  - <sup>15</sup> K. F. Mak, C. Lee, J. Hone, J. Shan, and T. F. Heinz, *Phys. Rev. Lett.*, **105**, 136805(2010).
  - <sup>16</sup> S. K. Mahatha, K. D. Patel, and K. S. Menon, *J. Phys.: Condens. Matt.*, **24**, 475504(2012).
  - <sup>17</sup> S. H. EI-Mahalawy and B. L. Evans, *Phys. Stat. Solidi. (b)*, **79**, 713 (1977).
  - <sup>18</sup> I. G. Lezama, A. Arora, A. Ubaldini, C. Barreteau, E. Giannini, M. Potemski, and A. F. Morpurgo, *Nano letters*, **15**, 2336 (2015).
  - <sup>19</sup> K. F. Mak, K. He, J. Shan, and T. F. Heinz, *Nat. Nanotechnol.*, **7**, 494 (2012).
  - <sup>20</sup> D. Xiao, G. B. Liu, W. Feng, X. Xu, and W. Yao, *Phys. Rev. Lett.* **108**, 196802 (2012).
  - <sup>21</sup> T. Cao, G. Wang, W. P. Han, H. Q. Ye, C. R. Zhu, J. R. Shi, Q. Niu, P. H. Tan, E. G. Wang, B. L. Liu, and J. Feng, *Nat. Commun.* **3**, 887 (2012).
  - <sup>22</sup> N. Ma and D. Jena, *Appl. Phys. Lett.* **102**, 132102 (2013).
  - <sup>23</sup> C. Ruppert, O. B. Aslan, T. F. Heinz, *Nano Lett.* **14**, 6231 (2014).
  - <sup>24</sup> N. R. Pradhan, D. Rhodes, S. Feng, Y. Xin, S. Memaran, B. H. Moon, H. Terrones, M. Terrones, L. Balicas, *ACS Nano* **8**, 5911 (2014).
  - <sup>25</sup> S. Cho, S. Kim, J. H., Kim, J. Zhao, J. Seok, D. H. Keum, J. Baik, D. Choe, K. J. Chang, K. Suenaga, S. W. Kim, Y. H. Lee, and H. Yang, *Science*, **349**, 625 (2015).
  - <sup>26</sup> W. Shi, J. Ye, Y. Zhang, R. Suzuki, M. Yoshida, J. Miyazaki, N. Inoue, Y. Saito, and Y. Iwasa, *Sci. Rep.*, **5**, 12534 (2015).
  - <sup>27</sup> L. Hromadová, R. Martoňák, and E. Tosatti, *Phys. Rev. B*, **87**, 144105 (2013).
  - <sup>28</sup> Z. H. Chi, X. M. Zhao, H. Zhang, A. F. Goncharov, S. S. Lobanov, T. Kagayama, M. Sakata, and X. J. Chen, *Physical review letters*, **113**, 036802 (2014).
  - <sup>29</sup> Z. H Chi, X. L. Chen, F. Yen, F. Peng, Y. H. Zhou, J. L. Zhu, Y. J. Zhang, X. D. Liu, C. L. Lin, S. Q. Chu, Y. C. Li, J. G. Zhao, T. Kagayama, Y. M. Ma, and Z. R. Yang, *Phys. Rev. Lett.*, **120**, 037002(2018).
  - <sup>30</sup> M. Rifiková, R. Martoňák, and E. Tosatti, *Phys. Rev. B*, **90**, 035108 (2014).
  - <sup>31</sup> O. Kohulák and R. Martoňák, *Phys. Rev. B*, **95**, 054105(2017).
  - <sup>32</sup> A. G. Gavriliuk, A. A. Mironovich, and V. V. Struzhkin, *Rev. Sci. Instrum.* **80**, 043906 (2009).
  - <sup>33</sup> H. K. Mao, P. M. Bell, J. W. Shaner, and D. J. Stembey, *J. Appl. Phys.* **49**, 3276 (1978).
  - <sup>34</sup> G. Kresse and J. Furthmüller, *Phys. Rev. B*, **54**, 11169 (1996).
  - <sup>35</sup> P. Blöchl, *Phys. Rev. B*, **50**, 17953 (1994).
  - <sup>36</sup> J. P. Perdew, *Phys. Rev. B*, **45**, 13244 (1992).
  - <sup>37</sup> J. P. Perdew, K. Burke, and M. Ernzerhof, *Phys. Rev. Lett.*, **77**, 3865 (1996).
  - <sup>38</sup> Z. Zhao, H. Zhang, H. Yuan, S. Wang, Y. Lin, Q. Zeng, G. Xu, Z. X. Liu, G. K. Solanki, K. D. Patel, Y. Cui, H. Y. Hwang, and W. L. Mao, *Nat. Commun.*, **6**, 7312 (2015).
  - <sup>39</sup> A. P. Nayak, Z. Yuan, B. X. Cao, J. Liu, J. J. Wu, S. T.

- Moran, T. S. Li, D. J. Akinwande, C. Q. Jin, and J. F. Lin, *ACS nano*, **9**, 9117 (2015).
- <sup>40</sup> Z. Y. Cao, J. W. Hu, A. F. Goncharov, and X. J. Chen, *Phys. Rev. B*, **97**, 214519 (2018).
- <sup>41</sup> N. R. Pradhan, D. Rhodes, S. Feng, Y. Xin, S. Memaran, B. H. Moon, H. Terrones, M. Terrones, and L. Balicas, *ACS Nano*, **8**, 5911 (2014).
- <sup>42</sup> N. R. Pradhan, D. Rhodes, Y. Xin, S. Memaran, L. Bhaskaran, M. Siddiq, S. Hill, P. M. Ajayan, and L. Balicas, *ACS Nano*, **8**, 7923 (2014).
- <sup>43</sup> H. Y. Chang, W. Zhu, D. Akinwande, *Appl. Phys. Lett.* **104**, 113504 (2014).
- <sup>44</sup> B. Chamlagain, Q. Li, N. J. Ghimire, H. J. Chuang, M. M. Perera, H. Tu, Y. Xu, M. H. Pan, D. Xaio, J. Q. Yan, D. Mandrus, and Z. X. Zhou, *ACS Nano*, **8**, 5079 (2014).
- <sup>45</sup> S. Sugai and T. Ueda, *Physical Review B*, **26**, 6554(1982).
- <sup>46</sup> X. F. Fan, D. J. Singh, Q. Jiang and W. T. Zheng, *Phys. Chem. Chem. Phys.*, **18**, 12080(2016).
- <sup>47</sup> F. Birch, *Phys. Rev.* **71**, 809 (1947).